Journal of Catalysis **206,** 98–113 (2002)
doi:10.1006/jcat.2001.3468, available online at http://www.idealibrary.com on IDEAL®

Selective Catalytic Reduction of Nitric Oxide by Ammonia over Egg-Shell MnO_x/NaY Composite Catalysts

M. Richter,*,[1] A. Trunschke,* U. Bentrup,* K.-W. Brzezinka,† E. Schreier,* M. Schneider,* M.-M. Pohl,* and R. Fricke*

*Institute for Applied Chemistry Berlin-Adlershof, Richard-Willstätter-Str. 12, D-12489 Berlin, Germany; and †Federal Institute for Materials Research and Testing (BAM), Richard-Willstätter-Str. 11, D-12489 Berlin, Germany

Received July 31, 2001; revised November 5, 2001; accepted November 5, 2001; published online January 14, 2002

A novel composite catalyst system for the selective catalytic reduction (SCR) of NO_x by NH_3 is described operating at temperatures lower than 470 K in the presence of water with NO conversions of 80–100% at space velocities of 30,000–50,000 h^{-1}. The catalyst is prepared by egg-shell precipitation of MnO_2 on the external surface of zeolite NaY. Structural and thermal stability of precipitated MnO_2 as well as of the MnO_2/NaY composite catalyst were characterized by N_2 adsorption, X-ray diffraction, laser Raman spectroscopy, temperature-programmed reduction, and electron microscopy. MnO_2 precipitated on zeolite NaY (15 wt% loading) retained its amorphous state up to calcination temperatures of 775 K. The zeolite component remained structurally intact. Calcination at higher temperatures destroyed the zeolite structure and transformed MnO_2 into Mn_3O_4. DRIFT spectroscopic investigations revealed the presence of symmetric O=N−O−N=O species formally corresponding to N_2O_3 on the composite catalyst after contact with NO. Catalytic measurements under integral flow conditions showed that the catalyst performance is associated with a close coupling of nitrite formation and its drain off from equilibria with NO/NO_2 and nitrate by ammonia. Several results are in line with the "diazotation" mechanism, including NH_3 protonation to NH_4^+, whereas prevailing Lewis acid sites should enable NH_3 activation via amide species, thus leading to a parallel "amide/nitrosamide" SCR reaction route. The activity-temperature profile fulfills the requirements of a low-temperature NO_x reduction catalyst for mobile diesel engines if an ammonia supply is implemented "on board," e.g., by urea decomposition.

Key Words: **SCR of NO_x by NH_3; egg-shell composite MnO_x/NaY catalyst; low-temperature activity; laser Raman spectroscopy; DRIFT spectroscopy; temperature-programmed reduction.**

INTRODUCTION

The selective catalytic reduction (SCR) of NO/NO_2 (NO_x) by NH_3 as reductant is the state-of-the-art technology for the abatement of nitrogen oxides from exhaust gases of stationary plants and combustion engines (1–3). The commonly used vanadia-based catalysts operate at temperatures between 575 and 725 K with high activity and selectivity. Over the last decade, the potential for the application of ammonia SCR to exhaust gas purification of diesel-driven vehicles has been investigated (4, 5). For mobile diesel engines the low NO_x emission limits of further legislative regulations can only be obeyed if the oxidation catalysts presently in use are supplemented by a NO_x reduction function. One strategy is to include the robust ammonia SCR technology into the exhaust gas aftertreatment of mobile diesel engines. Because the handling of toxic ammonia is problematic, the production of ammonia on board is preferred. This can be accomplished by thermal decomposition of urea. From several companies solutions are offered for heavy-duty engines (5, 6). However, for application of the urea SCR technology in diesel passenger cars, the volume of the catalyst system has to be minimized and the main SCR catalyst has to be active at exhaust gas temperatures of 425–525 K. This requires alternative catalysts with high intrinsic activity. The V_2O_5/TiO_2 catalyst commonly used for stationary SCR systems has insufficient performance at low temperatures. Much work has been focused on zeolite-based materials. While the application for lean-burn otto engines failed due to the limited hydrothermal stability of zeolites at the high exhaust gas temperatures of 700–1000 K normally encountered, the lower diesel exhaust gas temperatures do not exclude the application of zeolite-based catalysts. It is well-known that the SCR of NO_x by ammonia over nonmodified protonic zeolites or their ammonium forms is possible up to temperatures of 600 K (8–16). Interaction of ammonia with protonic zeolites leads to formation of ammonium ions fixed to the zeolite framework. It could be shown (17) that the reaction of ammonium ions with NO_x is stoichiometrically possible according to the equation

$$4\,Z^-NH_4^+ + 4\,NO + O_2 \rightarrow 4\,N_2 + 6\,H_2O + 4\,Z^-H^+, \quad [1]$$

where Z^- denotes the anionic zeolite framework. If no NH_3

[1] To whom correspondence should be addressed. Fax: +49 30 6392 4350. E-mail: mr@aca-berlin.de.

0021-9517/02 $35.00

is fed, the zeolite is converted into the protonic form and NO_x is reduced selectively to N_2. This transient reaction proceeds in dry gas atmosphere already at temperatures slightly above ambient. But the reaction rates are slow and complete NO_x conversion requires high residence times, i.e., low space velocities which are not appropriate for mobile diesel engines. Moreover, most studies of the NO_x SCR process by ammonia over zeolites have been performed with dry model exhaust streams. A reasonable performance was reported (9) for the conversion of ca. 480 ppm NO and 4 vol% O_2 with NH_3 preadsorbed on zeolite mordenite ($n_{Si}/n_{Al} = 5$). NO_x conversions amounted to 35% at 400 K and to 100% at 475 K at a space velocity of ca. 30,000 h^{-1} (9).

Nonmodified zeolites, however, are poor catalysts for the NO_x reduction in the presence of moisture, which is inevitably present in exhaust gas streams of combustion engines. Necessarily, the zeolites have to be promoted by components which accelerate one or more reaction steps, preferentially by the initial oxidation of NO to NO_2. Modification of the zeolite by ion exchange processes removes the protons and hence the Brønsted acidity of the zeolite matrix. This annihilates the beneficial influence of the Brønsted acid sites for storage and activation of NH_3 and decreases the low-temperature activity.

The approach we proposed (18, 19) was to combine the properties of the zeolitic component with the redox properties of a suitable manganese oxide without pore plugging of the zeolite in order to keep the interior available for deNO_x reaction steps. This has been achieved by precipitating an amorphous, mesoporous/macroporous MnO_x phase ($1.5 < x \leq 2.0$) on the external surface of zeolite microcrystals (18). It has been discussed in Ref. (17) that the ammonium form of the zeolite enables a cyclic operation with zeolite-fixed ammonium ions as reductant for gaseous NO_x. For high NO_x conversion, the close neighborhood of manganese oxide and zeolitic ammonium ions is indispensable (19). However, a deterioration of the catalyst performance was observed at longer time on stream in wet feed. A slight dealumination of the zeolite could be identified to be one reason for the capacity loss in NH_3 storage (18).

To improve the catalyst stability the sodium form of zeolite Y was chosen as catalyst component because of its higher hydrothermal stability. This results in a loss of the ability to fix gaseous ammonia in the form of ammonium ions and requires a permanent supply of ammonia reductant. In view of the application in exhaust gas cleaning of diesel internal combustion engines, thermal decomposition of urea is one alternative to providing ammonia on demand.

The present work aims at a more detailed understanding of the relevant factors determining the performance of the composite MnO_x/NaY catalyst in relation to its specific structure.

EXPERIMENTAL

Sample Preparation

The preparation of the composite catalyst is described in Ref. (18). The key step is the precipitation of MnO_2 according to Eq. [2] in aqueous solution in the presence of suspended zeolite powder.

$$3\,Mn(CH_3COO)_2 + 2\,KMnO_4 + 2\,H_2O \rightarrow 5\,MnO_2\downarrow + 4\,CH_3COOH + 2\,CH_3COOK \quad [2]$$

Commercial zeolite NaY (n_{Si}/n_{Al} atomic ratio = 2.3) (Aldrich) was suspended in distilled water at room temperature and MnO_2 precipitated in the presence of the zeolite by simultaneous admixture of Mn(II) acetate solution and $KMnO_4$ in stoichiometric concentrations to yield a MnO_2 loading of 15 wt%. From geometrical considerations, the amount of manganese oxide was chosen sufficiently high to guarantee a theoretical MnO_2 shell thickness around the zeolite microcrystals of about 1 μm. The suspension was heated to 353 K and kept at this temperature for an additional 30 min. As follows from Eq. [2] the residual solution contains diluted acetic acid and, hence, the pH value was found to be near 4. Nevertheless, it has been ascertained by ^{27}Al magic-angle spinning (MAS) NMR (18) that no acid leaching of tetrahedrally coordinated aluminum out of the zeolite lattice has occurred. After filtration and drying the solid was calcined at 773 K for 2 h in air (standard procedure). The calcination temperatures are indicated as subscripts (in K) of the sample designation chosen in accordance with that given in Ref. (18): 15 $MnNaY_{775}$ denotes the composite catalyst containing 15 wt% MnO_2 deposited on zeolite NaY, calcined at 775 K. Precipitated manganese (IV) oxide samples are abbreviated as Mn, with postcalcination temperatures given as subscripts. Textural data are summarized in Table 1. Reference crystalline manganese oxides were purchased from Alfa®, Germany.

Sample Characterization

Surface areas and pore volumes were determined by nitrogen adsorption on the ASAP 2010M facility (Micromeritics). Calculation of pore sizes followed the

TABLE 1

Textural Data of Samples

Sample	Surface area ($m^2\ g^{-1}$)	Micropore volume ($cm^3\ g^{-1}$)	Mesopore volume ($cm^3\ g^{-1}$)
Mn_{425}	170	0.05	0.14[a]
Mn_{775}	27	0.02	0.17[b]
15 $MnNaY_{775}$	664	0.28	0.11
NaY_{775}	928	0.44	—

[a] Average pore diameter, 3.3 nm.
[b] Cumulative volume of pores between 1 and 300 nm diameter.

method of Barrett-Joyner-Halender (20) according to implemented software routines.

X-ray diffraction (XRD) powder diffraction measurements were carried out with a STOE powder diffraction system using Cu K_α radiation. Reference spectra were taken from the ASTM data base.

Laser Raman spectroscopic measurements were performed on a DILOR XY-Raman spectrometer equipped with a nitrogen-cooled charge-coupled devise multichannel detector and a BH2-Olympus microscope (microprobe technique, objective 50×) providing a laser beam focus of ca. 2 μm. The power transferred to the sample surface was 0.11–1.06 mW μm^{-2}. The spectra were taken within the range 100–1375 cm^{-1} and accumulation times of 100–600 s using the 514.5-nm Ar^+ line for excitation. The accuracy of band positions was checked using monocrystalline Si(100) that provides the Raman active Γ_{25} mode of Si at 520 cm^{-1} (21).

Diffuse reflectance Fourier transform (DRIFT) measurements were accomplished with a diffuse reflectance attachment coupled to a modified reaction chamber (Harrick). The spectra were collected on a spectrometer FTS-60A (Bio-Rad) at a resolution of 2 cm^{-1}. Some 256 scans have been accumulated. Before measurements, all samples were treated *in situ* with He at 425 K for 1 h and subsequently cooled to ambient temperature. Flow rates amounted to 20 cm^{-3} min^{-1} with the exception of catalyst 15 MnNaY, where 10 cm^{-3} min^{-1} was used. The concentration of NO was 5 vol%. For recording NO adsorption, the spectra of the samples pretreated at the same temperature were used for reference.

The Fourier transform infrared (FTIR) characterization of acidity by pyridine adsorption was carried out on a Bruker IFS 66 spectrometer (2 cm^{-1} resolution, 100 scans). The probe molecule pyridine (20 mbar) was adsorbed at room temperature until saturation on the sample powder pressed to self-supporting disks which were pretreated at 673 K under vacuum for 30 min. Results are presented as difference spectra obtained by subtraction of the spectrum of the pretreated sample at room temperature. Integrated absorbances were related to unit surface areas of the samples.

Temperature-programmed reduction (TPR) was achieved applying the characterization system AMI-1 (Altamira Instruments) equipped with a thermal conductivity detector. For reduction, a feed of 5 vol% H_2 in Ar was used at a heating rate of 5 K min^{-1}. The overall flow rate amounted to 25 cm^3 min^{-1}. The consumption of H_2 was determined from the integrated peak areas by calibration.

Electron microscopic images of samples were taken by scanning (SEM) as well as transmission-electron microscopy (TEM), applying an Amray 2000B microscope and a Philips CM20 at 200 kV (LaB_6), respectively. For TEM images, the samples were prepared by depositing the materials without any pretreatment on Lacey carbon films.

Catalytic Measurements

Catalytic measurements were performed in a flow system equipped with an integral flow reactor (internal diameter 10 mm) and online sampling system. Standard feed compositions comprised 1000 ppm NO, 1000 ppm NH_3, 10 vol% O_2, and 7 vol% H_2O at a space velocity of 48,000 cm^3 g_{cat}^{-1} h^{-1}. The apparent density of the composite catalysts amounted to ca. 0.5 g cm^{-3}, so that the true gaseous hourly space velocity (GHSV) amounts to 24,000 h^{-1}.

Analysis of the product flow was conducted using gas chromatography (HP 6890 series) on two parallel capillary columns linked to thermal conductivity detectors. A HP-PLOT MoleSieve column served for separation of N_2, O_2, and CO, and a Poraplot Q column for separation of NO, N_2O, H_2O, NH_3, and CO_2. Simultaneously, the exit stream composition was continuously analyzed by a multigas sensor (Multor 610, Maihak GmbH, Hamburg, Germany) equipped with nondispersive infrared channels for NO, CO, and SO_2 registration and a channel for electrochemical O_2 detection as well as with a NO_2/NO converter reducing NO_2 to NO over a molybdenum catalyst. The difference between overall NO_x and NO concentration corresponds to the NO_2 percentage.

Activity is expressed as the conversion of NO_x to N_2 at fixed experimental conditions. The N_2 selectivity of the reaction is defined as S (%) = 100 $[N_2])/([N_2]) + [N_2O])$. Formal reaction orders were determined from the linear fit of lg r vs lg c diagrams, where reaction rates r are derived from the variation of NO conversion with W/F_{NO} (W, catalyst weight; F_{NO}, NO feed rate) by numerical differentiation.

RESULTS

Structural Characterization of MnO_x and Composite Catalyst

XRD analysis. XRD diagrams of Mn_{425}, Mn_{775}, Mn_{875}, and Mn_{975} are shown in Figs. 1a–1d. Sample Mn_{425} is completely amorphous whereas Mn_{775} reveals diffraction lines attributable to α-MnO_2 (Fig. 1b). The intensity of the observed diffraction lines is low, and the percentage of crystallinity for the calcined sample is estimated to be ca. 15%. Samples Mn_{875} and Mn_{975} show additional diffraction lines attributable to γ-Mn_2O_3 (bixbyite-C). The intensity of the Mn_2O_3 lines increases with higher calcination temperature (cf. Figs. 1c and 1d).

Several modifications of MnO_2 and Mn_2O_3 phases are known (22) but all have in common the fact that the thermal conversion of MnO_2 phases proceeds via intermediate Mn_2O_3 to Mn_3O_4.

The XRD diagram of the composite 15 $MnNaY_{875}$ material shows exclusively reflections of the zeolite (Fig. 2A). A contribution from crystalline manganese oxide phases could not be resolved. Calcination of the composite catalyst

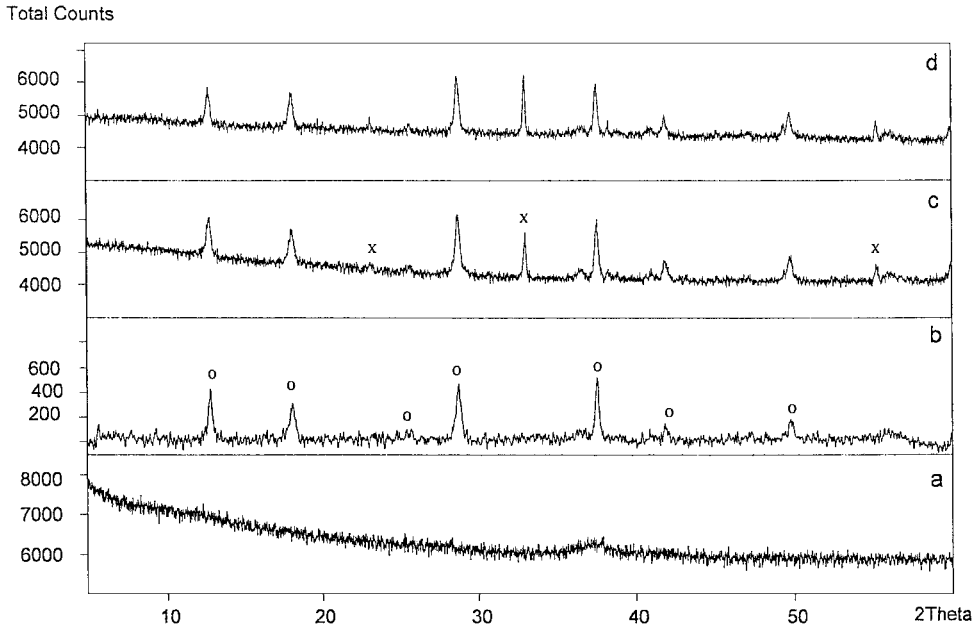

FIG. 1. XRD diagrams of precipitated samples Mn_{425} (a), Mn_{775} (b), Mn_{875} (c), and Mn_{975} (d). Reflections of α-MnO_2 and of γ-Mn_2O_3 (bixbyite-C) are marked by o and x, respectively.

at 975 K, however, leads to destruction of the zeolite crystallinity to a large extent and to conversion of the amorphous MnO_x phase into Mn_3O_4 (hausmannite), at least partially (Fig. 2B). This is different from the behavior of precipitated MnO_2 (cf. Fig. 1), where a mixture of Mn_2O_3 and MnO_2 is formed after calcination at 975 K. The fact that no Mn_3O_4 is observed for sample Mn_{975} is explained by a higher thermal stability of the γ-Mn_2O_3 phase formed, i.e., a higher crystallinity, whereas the γ-Mn_2O_3 phase of the composite catalyst is obviously in a more distorted state and more easily convertible to Mn_3O_4.

Laser Raman spectroscopy. Laser Raman spectra of samples Mn_{425}, Mn_{775}, and Mn_{975} are shown in Fig. 3A. Reference spectra of crystalline manganese oxides are given in Fig. 3B. The spectra were taken with low laser power (1 mW at maximum) to minimize thermal transformations of manganese oxides during spectrum accumulation.

The laser Raman spectra of the precipitated MnO_x samples reveal bands at 186, 271, 378, 474, 507, 579, and 632 cm^{-1}, with different intensities according to the calcination temperature. A comparison with reference spectra of crystalline manganese oxides (Fig. 3B) shows that the structure of unsupported precipitated MnO_x does not correspond to either crystalline β-MnO_2 (pyrolusite) (Fig. 3B,a), α-Mn_2O_3 (Fig. 3B,b) or Mn_3O_4 (Fig. 3B,c).

Amorphous MnO_2 is reported (23) to exhibit bands at ca. 510 and 580 cm^{-1}. A band observed at 633 cm^{-1} was assigned to γ-Mn_2O_3 with a distorted hausmannite structure by Bernard *et al.* (24), formed during spectrum acquisition by *in situ* decomposition of MnO_2 due to the high laser power applied (50 mW).

Bands at 507 and 579 cm^{-1} prove the existence of MnO_2. The band at 632 cm^{-1} is observed for all samples. A phase transformation *in situ* due to local heating is rather unlikely, because a laser power of only 1 mW has been used for spectrum acquisition. Hence, it has to be assumed that a distorted Mn_2O_3 phase not detectable by XRD is already present in sample Mn_{425}. Bands within the 182–187 cm^{-1} range for samples Mn_{775} and Mn_{975} point to the existence of γ-Mn_2O_3. A Raman line at 194–199 cm^{-1} is indicative for α-Mn_2O_3 (cf. Fig. 3B,b).

The spectra of Mn_{775} and Mn_{975} contain contributions from MnO_2 and Mn_2O_3. Considering XRD results, phase structures correspond to α-MnO_2 and γ-Mn_2O_3, respectively. No additional contributions from Mn_3O_4 were detected.

Laser Raman spectra of zeolite NaY and the composite material 15 $MnNaY_{775}$, the latter taken from sample regions differing in color, are shown in Fig. 4. Zeolite NaY has an intense white color under the microscope whereas sample 15 $MnNaY_{775}$ contains crystallites with grey–white to dark-brown color. The optical appearance of the sample under the microscope proves the deposition of manganese oxide on the zeolite microcrystals. But inhomogeneities of the coverage are evident. This is reflected by the modified laser Raman spectra according to the region they were taken from. The nonmodified NaY has its most intense Raman line at 501 cm^{-1}. This line is attributed to the symmetrical deformation (A1 symmetry) of the O atoms along the half angle of the T-O-T bridges (T = Si, Al) of the zeolite

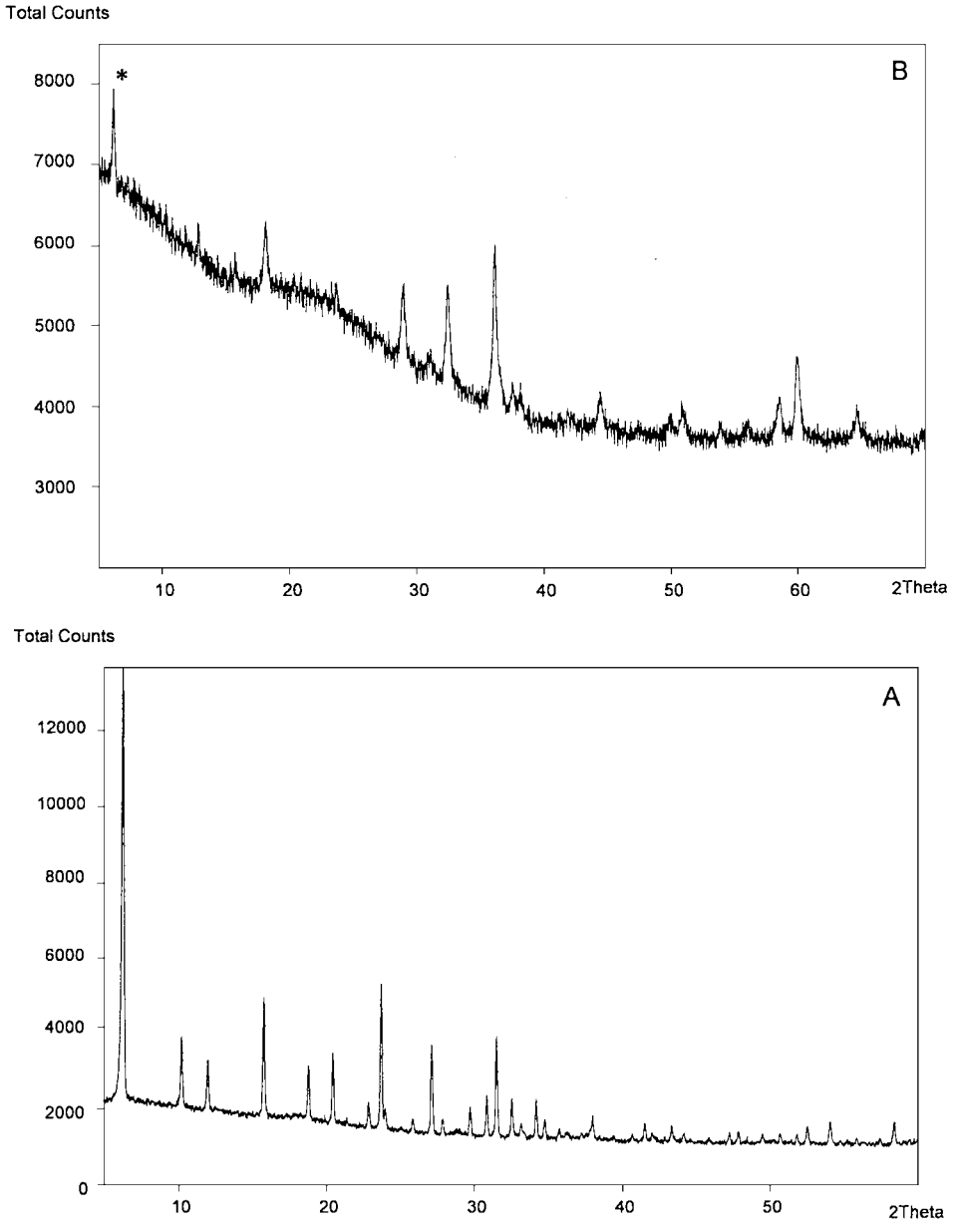

FIG. 2. XRD diagrams of samples 15 $MnNaY_{875}$ (A) and 15 $MnNaY_{975}$ (B). Residual zeolite reflections in (B) are marked by asterisks.

framework. Further Raman lines with lower intensity were found at 305, 359, 821, 1053, and 1113 cm^{-1}. The Raman spectra of the composite include contributions of the zeolite and the supported manganese oxide according to the local loading. The spectrum shown in Fig. 4b, taken from grey–white surface regions is dominated by the typical zeolite lines but additionally reveals two broad lines at 574 and 639 cm^{-1}. The manganese oxide layer is sufficiently thin to allow the acquisition of the zeolite spectrum in the grey–white and light-brown colored sample regions, which is not the case in the dark-brown colored regions. Raman lines of the zeolite are hardly recognizable in the spectrum shown in Fig. 4d, taken from dark regions of the sample surface. Instead, a band at 639 cm^{-1} dominates the spectrum, with a shoulder at 577 cm^{-1}. This corresponds to a mixture of MnO_2 and γ-Mn_2O_3 phases with varying proportions according to the local Mn loading on the zeolite microcrystals.

Temperature-programmed reduction. Reduction profiles for samples Mn_{425}, Mn_{575}, Mn_{775}, and 15 $MnNaY_{775}$ are shown in Fig. 5, together with those of reference samples. Reduction of samples Mn_{425} and Mn_{575} by H_2 starts at 375 K and proceeds almost identically in several superimposed processes. Formally, the profiles of samples Mn_{425} and Mn_{575} can be deconvoluted into four single processes (not shown). A clear modification of the TPR profile occurred

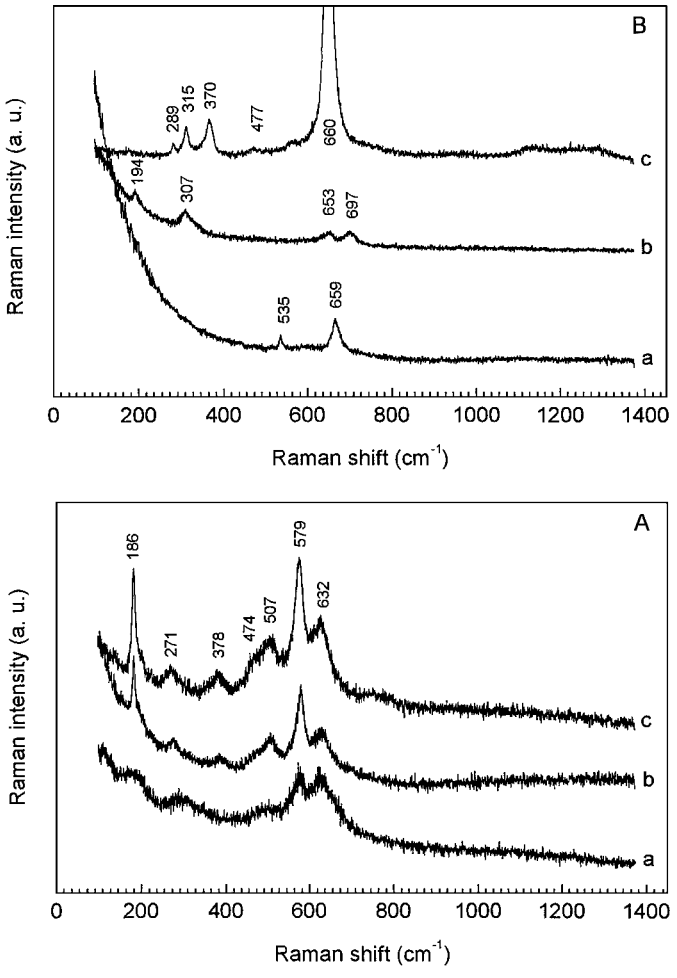

FIG. 3. Laser Raman spectroscopic characterization of (A) samples Mn_{425} (a), Mn_{775} (b), and Mn_{975} (c) and (B) reference crystalline manganese oxides β-MnO_2 (a), α-Mn_2O_3 (b), and Mn_3O_4 (c). Laser power, 1 mW; 600-s accumulation time; Ar^+ line excitation at 514.5 nm.

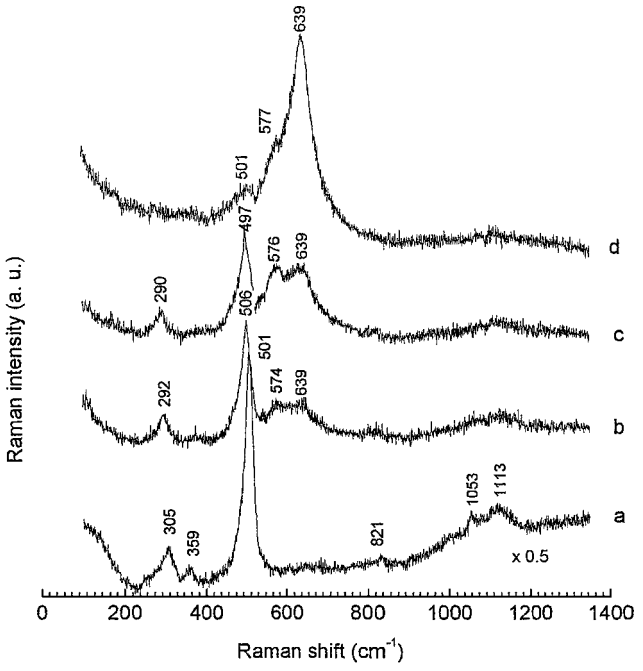

FIG. 4. Laser Raman spectra of zeolite NaY (a) and of sample 15 $MnNaY_{775}$ for different surface regions from (b) grey–white to (c) light-brown and (d) dark-brown appearance under the microscope.

for sample Mn_{775}. The onset of reduction is shifted to higher temperatures (around 525 K). The reduction of sample Mn_{775} by H_2 proceeds in one sharp peak centered at 580 K. The profiles of all three samples are different from those observed for crystalline β-MnO_2, α-Mn_2O_3, and Mn_3O_4 reference oxides (Figs. 5e–5g).

Reduction of precipitated MnO_x samples starts at lower temperatures compared with the crystalline oxide β-MnO_2. The reduction profile of crystalline β-MnO_2 revealed two overlapping peaks centered at 620 and ca. 670 K, which is in good agreement with results reported by Kapteijn *et al.* (25). The two-peak pattern is interpreted as stepwise reduction of MnO_2 to MnO via intermediate Mn_2O_3 or Mn_3O_4.

Formal reduction degrees calculated as a ratio between experimentally determined H_2 consumption and the H_2 consumption that is theoretically possible assuming MnO as the end product are summarized in Table 2. Nearly identical overall H_2 consumptions were found for Mn_{425}, Mn_{575}, and Mn_{775}. Obviously, no thermal loss of oxygen occurred during calcination up to 775 K. However, the overall H_2 consumption during TPR does not correspond to the hypothetical value of 0.5 mol of O_2 per mol of MnO_2. These low reduction degrees confirm the nonstoichiometric composition of the precipitated oxide. Stoichiometric reduction to MnO is fulfilled for crystalline commercial β-MnO_2, α-Mn_2O_3, and Mn_3O_4 with sufficient accuracy.

The TPR profile of sample 15 $MnNaY_{775}$ (Fig. 5d) agrees well with earlier measurements (18). It reveals a reducibility at relatively low temperatures comparable to the

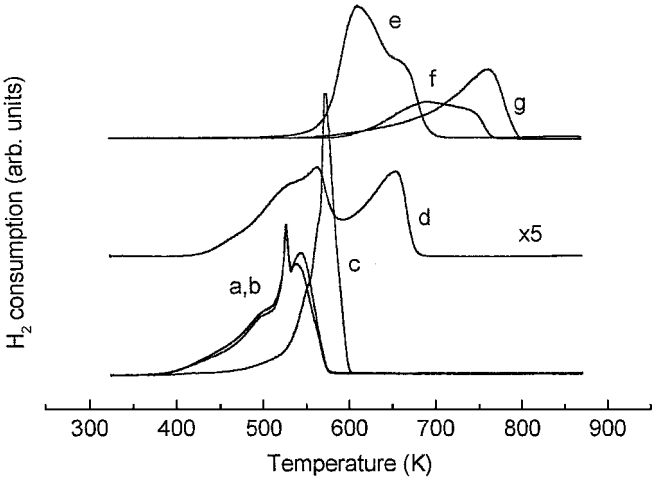

FIG. 5. H_2 consumption TPR profiles of samples Mn_{425} (a), Mn_{625} (b), Mn_{775} (c), and 15 $MnNaY_{775}$ (d) as well as of crystalline β-MnO_2 (e), α-Mn_2O_3 (f), and Mn_3O_4 (g). Profiles are vertically shifted for clarity.

TABLE 2

Reduction Degrees of Manganese Oxides and Sample 15 $MnNaY_{775}$ According to TPR

Samples	H_2 consumption (mmol g^{-1}), calc.[a]	H_2 consumption (mmol g^{-1}), exp.[b]	Reduction degree (%)
Mn_{425}	11.50	9.97	86.7
Mn_{575}	11.50	10.03	87.2
Mn_{775}	11.50	9.74	84.7
15 $MnNaY_{775}$	1.75	1.63	93.1
β-MnO_2	11.50	11.48	99.8
α-Mn_2O_3	6.33	6.42	101.4
Mn_3O_4	4.37	4.43	101.4

[a] Calculated for reduction to MnO for all samples.
[b] According to peak areas of the TPR profiles.

precipitated oxides Mn_{425} and Mn_{575}. This first reduction process between 425 and 600 K indicates a superimposition of at least two processes, resembling the behavior of the precipitated amorphous oxide. A second reduction peak not found for the unsupported oxides emerges between 600 and 700 K. The location on the temperature axis coincides with the second H_2 consumption peak observed for reduction of β-MnO_2 (Fig. 5e). But as long as the consecutive reduction process of the MnO_x phase mixture is not clarified, assignments of single reduction peaks to phase transformations are not justified.

The overall H_2 consumption of sample 15 $MnNaY_{775}$ is higher than for the unsupported oxide (cf. Table 2) but, nevertheless, does not correspond to a stoichiometric reduction of MnO_2 to MnO. This confirms the nonstoichiometric character of the manganese oxide. But the MnO_x phase supported on the zeolite support has higher thermal stability. In comparison, calcination of sample Mn_{775} initiated thermal decomposition and crystallization of γ-Mn_2O_3, thus leading to lower H_2 consumption during TPR.

Acidity characterization with pyridine as probe molecule. Gaseous pyridine interacts with both Brønsted and Lewis acid sites of solid materials. A differentiation is readily possible by IR spectroscopy. Pyridine adsorbed at Brønsted sites of a solid material forms PyH^+ ions with characteristic vibration bands at about 1540 and 1640 cm^{-1}, but if coordinatively bound to Lewis sites, bands at 1440–1460, 1488, and 1580–1630 cm^{-1} appear. FTIR spectra of zeolite NaY and the composite catalyst 15 $MnNaY_{775}$ after pyridine adsorption at room temperature and outgassing at 673 K under vacuum for 30 min are displayed in Fig. 6. Exclusively, the spectra reveal vibration bands of pyridine coordinated to Lewis acid sites. The dependence of the integral intensities of the Lewis band at 1442 cm^{-1} normalized to the surface area is shown in Fig. 7. Thermal desorption of pyridine occurs at temperatures higher than 475 K. Beneath this temperature, pyridine is stably coordinated to Lewis acid sites. Within the low-temperature region, the density of Lewis

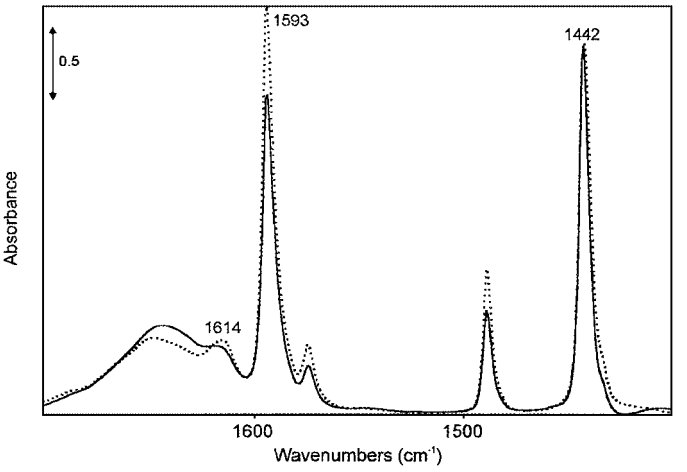

FIG. 6. FTIR spectroscopic acidity characterization of zeolite NaY (dotted line) and of sample 15 $MnNaY_{775}$ (solid line) by pyridine as probe molecule at room temperature (samples evacuated at 673 K for 30 min).

acid sites per unit of surface area is higher for the composite catalyst than for zeolite NaY. The higher density of Lewis acid sites found for the composite material implies that the MnO_x phase possesses its own Lewis acidity. The maximum at 475 K observed for NaY cannot be interpreted so far.

Electron microscopy. Electron microscopic images (SEM) taken from sample Mn_{775} and from the composite catalyst 15 $MnNaY_{775}$ showed that the precipitated MnO_x forms agglomerates consisting of small primary particles of 1 μm size or less whereas the micrograph of the catalyst is dominated by zeolite crystals of cubic shape and a size of 2–3 μm. The loading of the zeolite crystals by MnO_x is not resolved. A TEM image of the composite catalyst showed that the MnO_x particles are arranged around the zeolite crystals but do not form a coherent shell. Rather, patches of

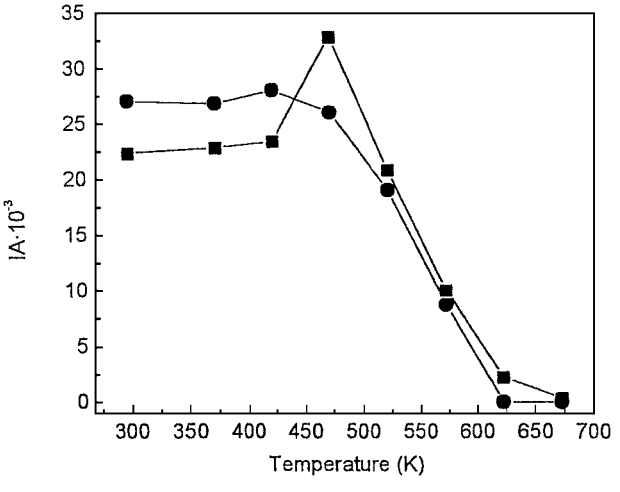

FIG. 7. Integrated IR absorbances of pyridine fixed to Lewis acid sites of (●) 15 $MnNaY_{775}$ and of (■) NaY vs sample temperature.

deposited manganese oxide are recognizable. Other parts of the manganese oxide are loosely accumulated near the zeolite surface. This explains the variations in laser Raman spectra depending on the position of the microscope above the catalyst surface.

Interaction of NO with MnO_x and the Composite Catalyst

DRIFT measurements were applied for characterizing surface species during interaction of NO with MnO_x and the composite catalyst. The DRIFT spectrum (not shown) of Mn_{425} annealed in the IR cell at 425 K under a flow of He for 1 h shows the presence of molecularly adsorbed water and adsorbed CO_2, as well as residual carbonate species. Obviously, the mild annealing at 425 K is not sufficient for removing these species from the surface completely. Mn–O vibrations that are located within the range 700–400 cm^{-1} (26, 27) cannot be seen due to the poor reflection of the dark-colored sample at wavenumbers below 1000 cm^{-1}.

Immediately after addition of NO to Mn_{425} at 298 K, one absorption band at 1208 cm^{-1} developed whose intensity does not change with a longer time of interaction (Fig. 8A). Further bands emerge at 1400 and 1326 cm^{-1}. The intensity of the band at 1326 cm^{-1} increases with time of NO interaction and the band position is shifted to 1315 cm^{-1}. Simultaneously, the band at 1400 cm^{-1} is transformed into a peak at 1419 with a shoulder at 1395 cm^{-1}. These bands indicate the presence of nitrite species (surface nitrito and nitro complexes) (27). If nitrates are coordinated to manganese ions in the chelating bidentate form (cf. Table 3) bands around 1290 and 1555 cm^{-1} should be present in the IR spectrum (28). Bridging bidentate nitrato species would cause a high-frequency absorption at a wavenumber higher than 1600 cm^{-1} (27). A weak absorption is seen in this region. Additionally, the weak band at 1038 cm^{-1} which emerges after 5 min of NO interaction is attributable to the ν_1 vibration of those nitrates. The band at 1208 cm^{-1} is difficult to assign. In Ref. (28) a band at 1230 cm^{-1} is attributed to bridging bidentate nitrito complexes. Bulk monodentate nitrito complexes are characterized by vibration bands in the spectral regions 1206–1065 and 1470–1375 cm^{-1} (26). Bridging nitro–nitrito complexes possess bands at 1260–1180 and 1520–1390 cm^{-1} (27). Therefore, it is reasonable to assume that bridging nitro–nitrito species are formed after interaction of NO with Mn_{425} at room temperature. The bands at 1315 and 1419 cm^{-1} are due to nitro complexes, whose formation proceeds slowly (29). The formation may cause a reduction according to Eq. [3],

$$2\,Mn^{n+} + NO + H_2O \rightarrow 2\,Mn^{(n-1)+} + NO_2^- + 2\,H^+, \quad [3]$$

where n may be 4 or 3 according to the valence state of interacting manganese ions. Three-valent manganese ions are likely present, as follows from the nonstoichiometric composition of the MnO_2 phase. Evidence for the reduction

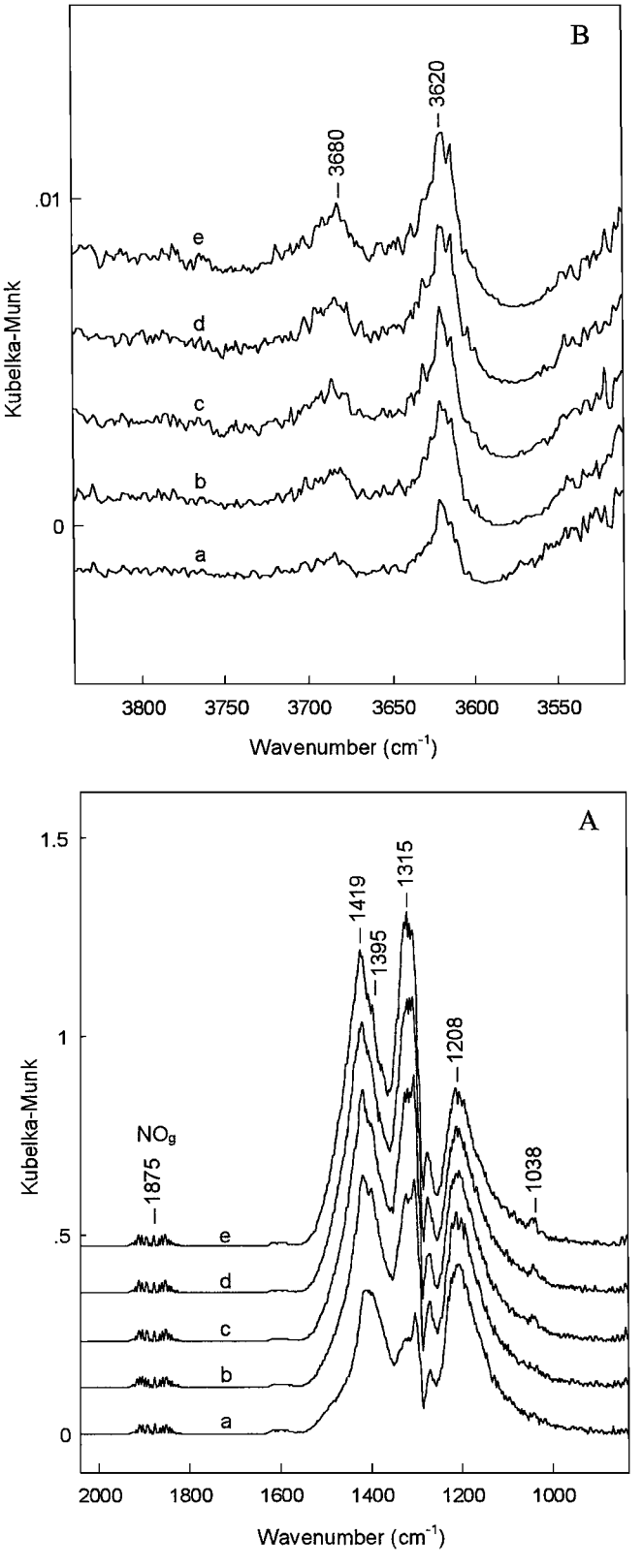

FIG. 8. Interaction of 5 vol% NO/He with sample Mn_{425} at 298 K. DRIFT spectra at progresive times of interaction. (a) Immediately after contact, and after (b) 5, (c) 10, (d) 15, and (e) 20 min. (A) Spectral region 2000–800 cm^{-1}; (B) hydroxyl region.

TABLE 3

Species Formed after Interaction of NO_x with Metal Cations (M) and Characteristic IR Vibration Frequencies

Species	Structural sketch	Main vibrational frequencies	Reference
Chelating bidentate nitrato	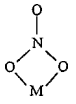	1500–1565 1260–1300	26, 30
Bridging bidentate nitrato	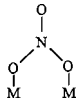	1600–1650 1170–1225	26
Bridging bidentate nitrito		ν_{as} (NO_2) 1266–1314 ν_s (NO_2) 1176–1203	26, 27
Monodentate nitrito	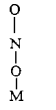	ν (N–O) 1065–1206 ν (N=O) 1375–1470	27
Bridging nitro nitrito		ν (N–O) 1180–1260 ν (N=O) 1390–1520	27
Nitro		ν_{as} (NO_2) 1375–1650 ν_s (NO_2) 1250–1350	26, 29

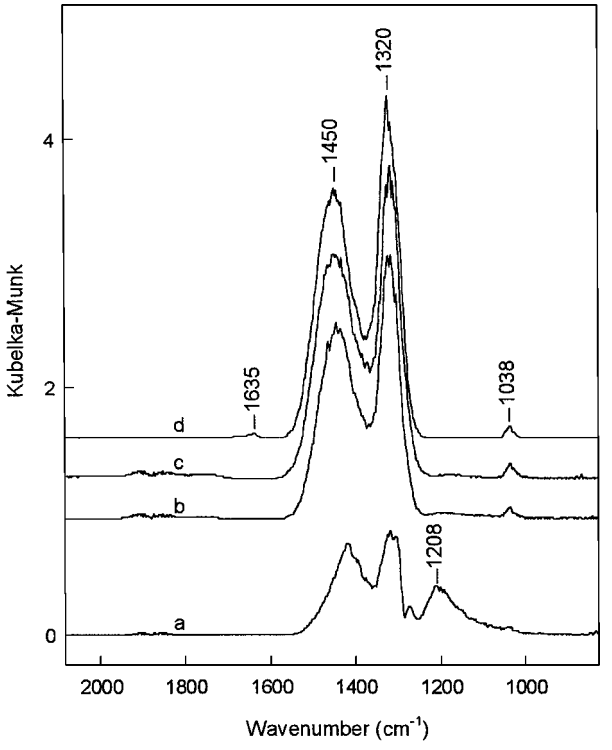

FIG. 9. Interaction of 5 vol% NO/He with sample Mn_{425}. DRIFT spectra at (a) 298, (b) 373, and (c) 423 K and (d) after cooling to 298 K under He flow. Time of contact, 20 min.

process (Eq. [3]) is provided by spectra shown in Fig. 8B, where the protonation of the surface leads to the emergence of OH groups linked to Mn (bands at 3680 and 3620 cm^{-1}).

A temperature increase leads to the following modifications of the spectrum (Fig. 9). The intensity of the band at 1208 cm^{-1} decreases and the intensity of bands attributed to nitro species increases. After cooling to room temperature, the spectrum is characterized by absorption of nitro complexes at 1450 and 1320 cm^{-1}, bridging bidentate nitrato complexes at 1038 cm^{-1} (weak), OH groups at 3680 and 3620 cm^{-1}, and adsorbed water (superimposed to nitrate) at 1635 cm^{-1}. The observed species are different from those reported in the literature for Mn_2O_3 and MnO_x/Al_2O_3 (28) or Mn–ZSM-5 (31).

Figure 10 compares the DRIFT spectra of NaY_{775}, Mn_{425}, and 15 $MnNaY_{425}$ after admission of NO at 298 K in the 1500–2200 cm^{-1} region. Nitrosyls of Mn^{n+} cations that produce bands in the 1750–1966 cm^{-1} region (26) were not formed. Different from NaY_{775} and Mn_{425}, sample 15 $MnNaY_{425}$ developed two weak bands at 1685 and 1664 cm^{-1} at 298 K. These bands may be attributed to the in-phase and out-of-phase motions of linked N=O stretch motions, which could indicate the presence of symmetric O=N–O–N=O species (30) formally corresponding to N_2O_3. The spectral region below 1400 cm^{-1} is not suitable for discussion because of the dominating strong absorption of the catalyst itself under the NO/He flow.

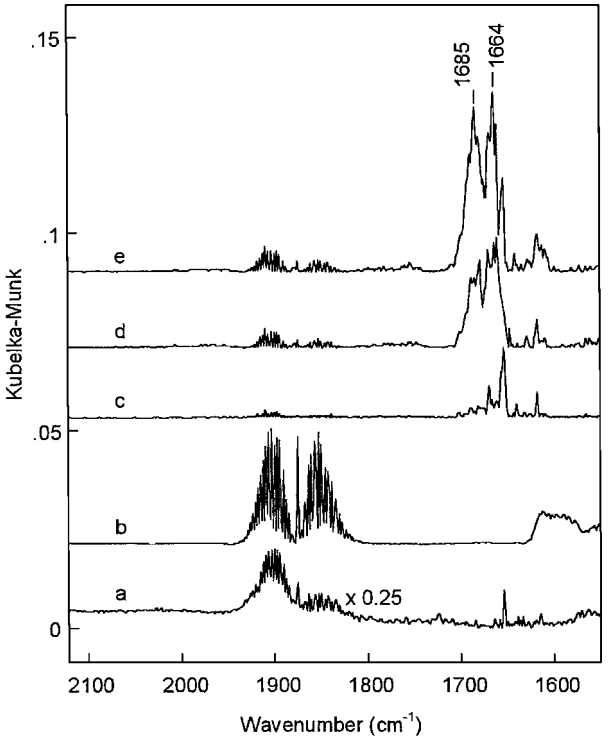

FIG. 10. DRIFT spectra of sample NaY_{775} (a) and sample Mn_{425} (b) after 5 min of interaction with 5 vol% NO/He at 298 K and of sample 15 $MnNaY_{425}$ after 1 (c), 5 (d), and 20 min (e).

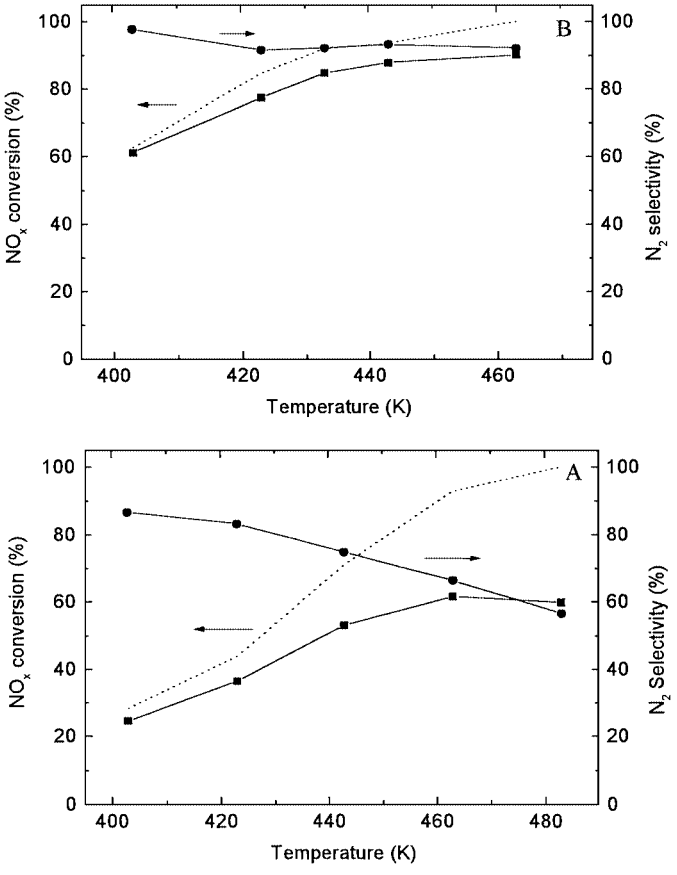

FIG. 11. SCR of NO_x by NH_3 over Mn_{775} (A) and over 15 $MnNaY_{775}$ (B) vs reaction temperatures. NO conversion to N_2 (■) and overall conversion (dotted line). Selectivity of N_2 formation (●). Reaction conditions: 1000 ppm NO, 1000 ppm NH_3, 10 vol% O_2, 7 vol% H_2O. SV = 48,000 $cm^3\ g_{cat}^{-1}\ h^{-1}$.

Catalytic Properties

Steady state SCR of NO_x. Results of measurements for sample Mn_{775} and the composite catalyst 15 $MnNaY_{775}$ performed with standard feed composition at a space velocity (SV) of 48,000 $cm^3\ g_{cat}^{-1}\ h^{-1}$ within the temperature range 400–500 K are shown in Figs. 11A and 11B, respectively. The overall NO_x conversion over Mn_{775} increases from 30% at 413 K to 100% at 485 K. However, the N_2 selectivity of the NO_x conversion is poor. Nearly 50% of NO_x is converted to N_2O at 483 K. This finding is in line with results reported by Kapteijn *et al.* (25), who also found a high percentage of side reaction to N_2O for the SCR of NO_x over pure manganese oxides. At the same experimental conditions, the composite catalyst 15 $MnNaY_{775}$ reveals both higher activity for the SCR of NO_x and higher selectivity to N_2 (Fig. 11B) compared with sample Mn_{775}. Table 4 summarizes relevant reaction data for 15 $MnNaY_{775}$ in comparison with literature data for Mn-based SCR catalyst systems. Most published data have been obtained with dry feed. This allows high conversions at low temperatures but the catalyst performance is not relevant for real wet exhaust. With wet exhaust gas compositions (7 vol% H_2O) the composite standard catalyst 15 $MnNaY_{775}$ achieves an average NO_x conversion of 70% at 423 K over at least 70 h time-on-stream (TOS) and, hence, is more efficient than the other cited Mn-based catalysts.

Influence of feed composition. Three feed variants were considered at a reaction temperature of 423 K: 1000 ppm NO_2, 500 ppm NO/500 ppm NO_2, and 1000 ppm NO/10 vol% O_2, each completed by addition of 1000 ppm NH_3 and 7 vol% H_2O as well as He for dilution. Results are shown in Fig. 12.

The highest NO_x conversion to N_2 of ca. 80% is observed with a feed containing equimolar amounts of NO and NO_2, and the lowest NO_x conversion to N_2 (ca. 50%) with a feed containing exclusively NO_2. Regarding formation of N_2, results for the NO/O_2 feed are comparable with those for the NO/NO_2 feed. These findings confirm that a mixture of NO/NO_2 is beneficial to the reaction. Formally, an equimolar mixture of NO/NO_2 corresponds to N_2O_3, the source of NO_2^- anions in contact with moisture. Nitrite is viewed as the intermediate species leading to N_2 in the reaction course (see later). Obviously, the good performance of the composite catalyst is related to the ability to produce NO_2 in sufficient concentration by oxidation of NO, thus providing a NO/NO_2 mixture. Therefore, comparable NO_x conversions to N_2 are achieved in comparison with the NO/NO_2 premixed feed. With all feed compositions, N_2O was found in comparable concentrations of ca. 100 ppm. N_2O originates from decomposition of ammonium nitrate, which is formed if intermediate nitrite is converted to nitrate and residual ammonia is present (conversion levels less than 100%).

Oxidation of NO by gaseous O_2. Conversion of NO to NO_2 by wet and dry air over the composite catalyst is shown in Fig. 13 in dependence on the reaction temperature, together with the observed level of homogeneous NO oxidation proceeding in the connection lines and in the free reactor volume. The homogeneous oxidation amounts to about 10%, whereas conversions from 60 to 80% are observed with dry feed in the presence of the catalyst. The dependence of NO conversion on temperature proceeds through a minimum between 350 and 400 K with dry feed.

This was earlier reported for pure zeolites by Halasz *et al.* (39) and attributed to a superimposition of thermodynamic and kinetic contributions. At low temperature, the adsorption equilibrium of NO is decisive for the catalytic transformation to NO_2. This adsorption equilibrium is shifted to the gas phase if temperatures exceed 375–400 K, and the oxidation of NO to NO_2 becomes kinetically controlled. At higher temperatures (>600 K) the NO/NO_2 equilibrium limits the maximum conversion of NO.

TABLE 4

Stationary Conversion of NO_x by NH_3 over Mn-Based Catalysts

Catalyst	Feed composition				Reaction conditions					Reference
	NO (ppm)	NH_3 (ppm)	O_2 (%)	H_2O (%)	T (K)	X_{NO_x} (%)	S_{N_2} (%)	SV ($cm^3\ g^{-1}\ h^{-1}$)	TOS (h)	
Pure bulk Mn oxide[a] MnO_2	500	550	2	0	383 398 423 473	60 70 92 90	90 82 75 38	?[b]	15	25
Mn/γ–Al_2O_3 (2 wt% Mn)	500	550	2	1–5	383–698	?[c]	?[c]	25,000	10–15	32
Mn/γ–Al_2O_3 (2 wt% Mn)	450	500	2	0	423	10 40 38	n.d.	31,000	65 100 150	33, 34
Mn/γ–Al_2O_3 (2 wt% Mn)	45	500	2 5	0	423	37 55	≈100	37,500		35
Mn_2O_3–WO_3/γ-Al_2O_3 (10.8/6.8/82.4 wt%)	550	500	10	0	398 423	25 45	100	91,400	3	36
MnO_x/Al_2O_3[d]	500	550	2	0	383 423 443 473	25 63 80 97	≈100 90 80 70	24,000		37
Mn/carbonized silica–alumina (2.5 wt% Mn, impregnated)	800	800	3	0	413 453 493 533 573	94 98 96 85 67	91 79 71 65 44	12,000		38
15 $MnNaY_{775}$	1000	1000	10	7	423	74 74 77 71 69	92 91 92 92	48,000	1 10 20 40 70	This work
15 $MnNaY_{775}$	1000	1000	10	7	443	88 82	93 93	48,000	22 32	This work
15 $MnNaY_{775}$	1000	1000	5	7	443	82	94	48,000	75–80	This work

[a] Further investigated oxides with lower activities but partly higher selectivities: Mn_5O_8, Mn_2O_3, Mn_3O_4.

[b] Only the feed rate was given: 50 $cm^3\ min^{-1}$.

[c] No conversion data given, but relative rate constants k/k_{ref}, related to reference values of the rate constant k_{ref} without water addition. Addition of 2 vol% H_2O leads to a reversible decrease from 1 to 0.3.

[d] Impregnation of commercial Al_2O_3 (55 $m^2\ g^{-1}$) with $HMnO_4$ solution and calcination at 423, 573, 873, and 1273 K for 5 h. Values are given for the sample calcined at 573 K. n.d., Not determined.

Oxidation of NH_3. The catalytic oxidation of NH_3 to N_2 is described to proceed on catalysts according to

$$4\,NH_3 + 3\,O_2 \rightarrow 2\,N_2 + 6\,H_2O \qquad [4]$$

but, particularly at higher temperatures, oxidation to NO takes place:

$$4\,NH_3 + 5\,O_2 \rightarrow 2\,NO + 6\,H_2O. \qquad [5]$$

Intermediate NO in the presence of O_2 and NH_3 corresponds to a gas composition containing all components for the SCR of NO_x by NH_3. Therefore, first traces of NO could effectively be converted to N_2 in the same way as with a feed containing NO a priori. This "internal" SCR is reported as the reaction route of NH_3 oxidation to N_2 by Amblard *et al.* (40). The N_2O formation might occur for the same reason as discussed before, indicating thermal decomposition of ammonium nitrate. Kapteijn *et al.* (25) considered the reaction

$$2\,NH_3 + 2\,O_2 \rightarrow N_2O + 3\,H_2O \qquad [6]$$

as the source for N_2O formation, dominating the oxidation of NH_3 over MnO_x at higher temperatures.

As follows from the reaction routes of NH_3 oxidation, the N balance of the NO_x reduction might be disguised if side

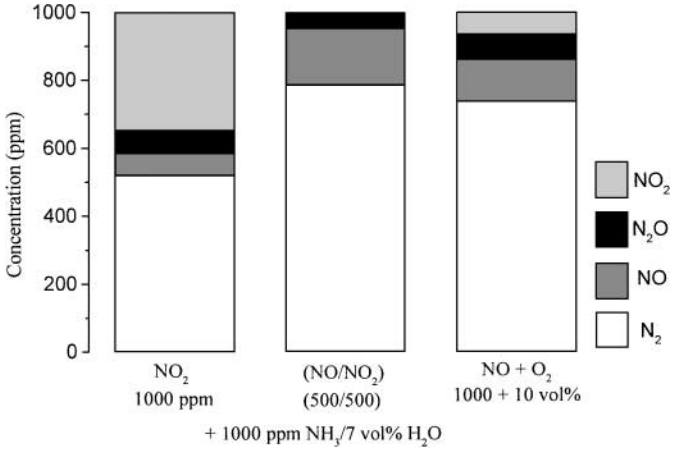

FIG. 12. Influence of feed composition on product distribution for the SCR of NO_x by NH_3 over 15 $MnNaY_{775}$ at 425 K. SV = 48,000 $cm^3\ g_{cat}^{-1}\ h^{-1}$.

reactions [4]–[6] accompany the NO_x conversion to relevant degrees. For this reason, the activity of the composite catalyst has been checked for its oxidation properties with a feed of 1000 ppm NH_3, 5 vol% O_2, and 7 vol% H_2O at standard space velocity.

Results are shown in Fig. 14. Oxidation of NH_3 is observed at temperatures higher than 450 K, leading to formation of N_2 and N_2O. The concentration of both products proceeds through a maximum located at about 600 K. Consumption of NH_3 is as high as 60% at this temperature. NO is detectable in the gas phase at higher temperatures.

Influence of reactant concentrations. The NO concentration has been varied by either keeping the NH_3 concentration constant, i.e., higher NO concentration causes a feed composition increasingly lean of NH_3, or by maintaining the n_{NO}/n_{NH_3} molar ratio at 1. This corresponds to the required reaction stoichiometry if the conversion runs in a

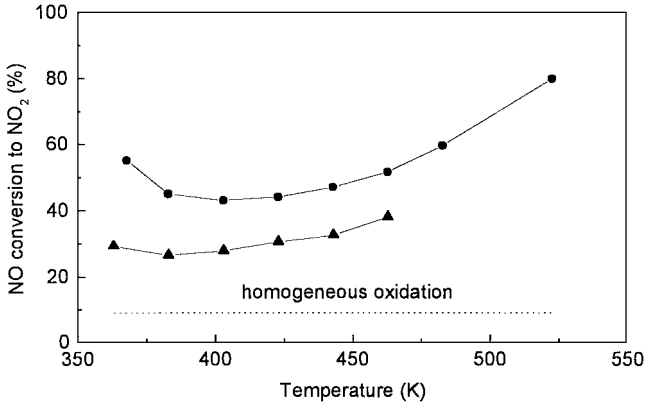

FIG. 13. Oxidation of NO to NO_2 over catalyst 15 $MnNaY_{775}$ in dry feed (●) and wet feed (▲). Feed composition: 1000 ppm NO, 10 vol% $O_2 \pm 7$ vol% H_2O. SV = 8000 $cm^3\ g_{cat}^{-1}\ h^{-1}$. (Dotted line) Homogeneous oxidation at a feed flow rate of 2 $cm^3\ s^{-1}$.

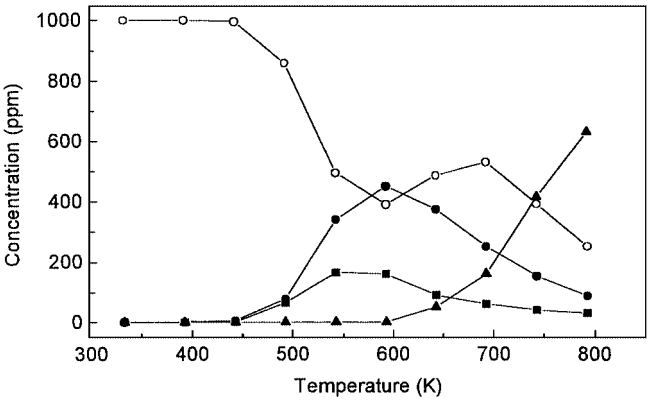

FIG. 14. NH_3 oxidation over catalyst 15 $MnNaY_{775}$ vs reaction temperature. Conditions: 1000 ppm NH_3, 5 vol% O_2, 7 vol% H_2O. SV = 48,000 $cm^3\ g_{cat}^{-1}\ h^{-1}$. (○) NH_3, (●) N_2O, (■) N_2, (▲) NO.

selective way according to Eq. [7]:

$$4\,NO + 4\,NH_3 + O_2 \rightarrow 4\,N_2 + 6\,H_2O. \qquad [7]$$

For both cases, conversion data of NO versus the NO concentration at a reaction temperature of 425 K are shown in Fig. 15A. A feed containing 1000 ppm of each reactant yields 86% of NO conversion. With 2000 ppm NO but n_{NO}/n_{NH_3} equal to 2, the conversion decreases considerably due to the nonstoichiometric low NH_3 concentration. On the other hand, at 500 ppm NO and a ratio of n_{NO}/n_{NH_3} of 0.5, the conversion of NO reaches 95%. If the NH_3 supply is correspondingly changed with the NO concentration fixing the n_{NO}/n_{NH_3} ratio at 1, there is practically no influence on the conversion of NO between 500 and 2000 ppm.

The influence of oxygen on the SCR of NO_x at reaction temperatures of 425, 445, and 455 K is shown in Fig. 15B. The influence persists over the investigated concentration range but is lower from 5 to 10 vol%. The reaction is promoted by enhanced O_2 concentration. At the highest O_2 content, NO_x conversion amounts to 86, 95, and 100% at 425, 445, and 455 K, respectively, with N_2 selectivities of 90% or higher.

For a reaction temperature of 425 K the influence of H_2O concentration has been investigated. The result shown in Fig. 15C provides evidence that the NO conversion to N_2 decreases from 90% at 6 vol% H_2O to ca. 60% at a water content of 30 vol%. Full conversion is achieved with dry feed.

Formal reaction orders. Formal reaction orders were determined from a logarithmic representation of NO consumption rates versus component concentrations. Figure 16 displays the result for variation of the NO concentration between 500 and 2000 ppm.

The linearization performed is valid for a simple power rate model

$$-r_{NO} = dX/d(W/F_{NO}) = k_{app.}\, c_{NO}^{n} \qquad [8]$$

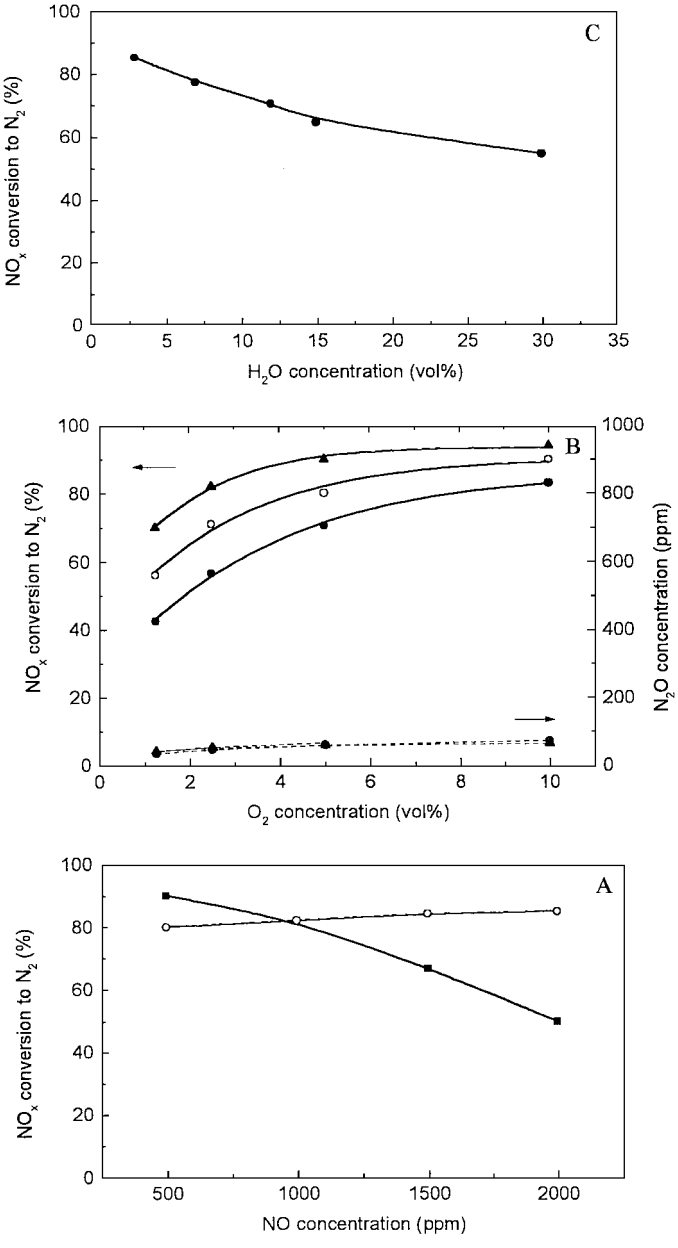

FIG. 15. SCR of NO_x by NH_3 over 15 $MnNaY_{775}$. Conversion of NO to N_2 in dependence on (A) NO concentration at $n_{NO}/n_{NH3} = 1$ (○) and at n_{NH3} = constant (1000 ppm) (■), T = 425 K; (B) O_2 concentration at 425 (●), 445 (○), and 455 K; and (C) H_2O concentration, T = 425 K. SV = 48,000 $cm^3\ g_{cat}^{-1}\ h^{-1}$.

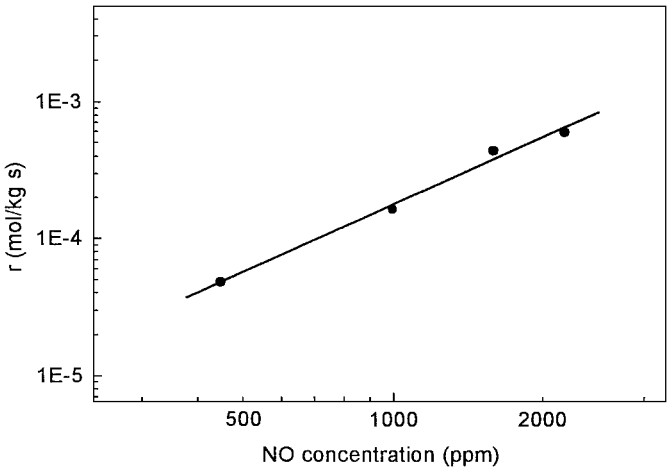

FIG. 16. Rate of NO consumption vs NO concentration for catalyst 15 $MnNaY_{775}$ in logarithmic coordinates. Reaction temperature, 425 K. Conditions: 500–2000 ppm NO, 1000 ppm NH_3, 10 vol% O_2, 7 vol% H_2O. SV = 48,000 $cm^3\ g_{cat}^{-1}\ h^{-1}$.

if gas-phase concentrations of all other components are kept constant. In Eq. [8], X denotes the NO conversion, W the catalyst weight, and F_{NO} the feed rate of NO. The apparent rate constant $k_{app.}$ comprises the true rate constant and the numerical contribution from fixed concentrations of other reaction partners; n is the integral reaction order of NO.

It turned out that the reaction order of NO is approximately 2. This reaction order is higher than reported by other authors. Overwhelmingly, orders of or near +1 are reported (8, 9, 14) independent of catalyst type and proposed reaction mechanism. A reaction order of 2 implies that two NO molecules are involved in the rate-limiting step. This is reconcilable with a mechanism where after fast initial oxidation of NO to NO_2 both molecules form an intermediate (formally N_2O_3) that reacts with NH_3. This conclusion is in line with the observed beneficial influence of a mixed NO/NO_2 feed on the SCR process.

The integral reaction order of oxygen is 0.3. No meaningful results could be obtained, however, for variation of H_2O and NH_3 concentrations. NH_3 in excess leads to balance discrepancies, pointing to formation of ammonium nitrate. H_2O variation in such large excess over NO and NH_3 has an overall deactivating effect on the NO_x conversion but its interference with the reaction kinetics is obviously not straightforward. Acquired reaction orders with standard deviations and correlation coefficients of the linear fit are summarized in Table 5.

DISCUSSION

It was shown in this article that zeolite NaY in conjunction with a precipitated nonstoichiometric MnO_2 phase

TABLE 5

Formal Reaction Orders of Components for the SCR of NO_x over 15 $MnNaY_{775}$ at 425 K

Component	n	Linear fit	SD[a]	Range
NO	1.8 ± 0.10	0.9955	0.06	500–2000 ppm
O_2	0.3 ± 0.02	0.9935	0.02	1.25–10 vol%

[a] Standard deviation.

represents a promising catalyst for the low-temperature SCR of NO_x by NH_3. Deposition of 15 wt% MnO_2 by precipitation reaction [2] on the external surface of zeolite NaY microcrystals leads to patches of amorphous MnO_x, as recognizable from TEM images, but does not completely cover the surface of the zeolite microcrystals. In the presence of excess gas-phase oxygen and water vapor, oxidation of NO to NO_2 proceeds to a considerable extent at reaction temperatures above 370 K. Without gas-phase oxygen, the participation of MnO_x bulk oxygen in NO oxidation to NO_2 could be proven to occur (18, 41). The redox activity of the MnO_x component provides a mixed NO/NO_2 feed, formally equivalent to N_2O_3. However, N_2O_3 is known as a very labile oxide decomposing easily to NO/NO_2 in the gas phase (Eq. [9]).

$$N_2O_3 \leftrightarrow NO + NO_2 \qquad [9]$$

Sultana *et al.* (42) showed recently that zeolite NaY is able to stabilize N_2O_3 inside the super cage by displacing water molecules adsorbed at Na^+ cations. The authors emphasized that this behavior of zeolite NaY is unique. Identification relies on the presence of IR absorption bands at 1270, 1590, and 1905 cm^{-1}. Szanyi and Paffett (43) attributed IR bands at 1587 and 1875 cm^{-1} observed for gas-phase spectra over zeolite H-ZSM-5 to N_2O_3. Similar assignments were given by other authors (e.g., Ref. (44)). DRIFT spectroscopic results obtained in the present work point to the existence of adsorbed N_2O_3 in a symmetric configuration. The configuration is thought as a specific coordination of two NO molecules to surface oxygen of the catalyst rather than to the existence of molecular N_2O_3, because NO was used in an inert He stream so that oxidation of NO by gas-phase oxygen could not take place. Most of literature results attributed IR bands to an asymmetric N_2O_3 configuration. The asymmetric N_2O_3 molecule is described as a NO molecule weakly linked to a NO_2 molecule (O=N–NO_2). Consequently, the stretching vibrations of asymmetric N_2O_3 are similar to the modes of NO and NO_2, which complicates the identification. In the presence of water, the equilibrium

$$2\,NO^+ + H_2O \leftrightarrow N_2O_3 + 2\,H^+ \qquad [10]$$

is suggested to exist (41, 44). Nitrosonium ions NO^+ and nitrate anions NO_3^- resulted from disproportionation of N_2O_4. N_2O_4 was observed after room temperature interaction of NO/O_2 with the catalyst (41). Moreover, both *in situ* FTIR investigations discussed in Ref. (41) and *in situ* DRIFT measurements of the present work confirmed the formation of nitrite and nitrate surface species. In the presence of moisture, interaction of N_2O_3 with water leads to nitrous acid (Eq. [11]).

$$N_2O_3 + H_2O \leftrightarrow 2\,HNO_2 \qquad [11]$$

Nitrous acid can disproportionate into nitric acid and nitric oxide according to Eq. [12].

$$3\,HNO_2 \leftrightarrow HNO_3 + 2\,NO + H_2O \qquad [12]$$

The same components are formed upon interaction of NO_2 with moisture (Eqs. [13] and [14]).

$$2\,NO_2 + H_2O \leftrightarrow HNO_2 + HNO_3 \qquad [13]$$

$$3\,NO_2 + H_2O \leftrightarrow 2\,HNO_3 + NO \qquad [14]$$

Conversions described by Eqs. [9]–[14] are equilibrium reactions. Therefore, several components may be present simultaneously in the gas phase during steady state catalysis. But the formation of nitrite (nitrous acid) and the transformation of nitrite to nitrate (nitric acid) are viewed as the key steps of the reaction. Reaction progress demands the efficient removal of nitrite before its reverse decomposition into NO/NO_2 (Eq. [9]) or its further transformation into nitrate (Eq. [12]). Practically, HNO_2 has to be drained off from the set of equilibrium reactions [11]–[13] by reaction with NH_3. It is reasonable to conclude from Eq. [14] that excess NO_2 enhances the nitrate (nitric acid) formation. Prevailing nitrate formation should diminish the conversion of NO to N_2. This is confirmed by results of feed variation presented in Fig. 12. A feed of NO_2 yielded a conversion of ca. 50% into N_2, which is far less than that observed for an equimolar NO/NO_2 mixture or for NO/O_2 over the composite catalyst. The comparable results achieved for NO/NO_2 and NO/O_2 feed compositions indicate the good oxidation capability of the manganese oxide for the catalytic conversion of NO to NO_2. Rate limitations should have kinetic reasons because, thermodynamically, NO_2 is favored at low temperatures and complete conversion of NO to NO_2 is achievable.

The high reaction order of NO near 2 confirms a reaction stoichiometry requiring formally two NO (NO/NO_2) molecules for the reaction to proceed. This is the prerequisite for nitrite formation and supports the conclusion that the diazotation mechanism

$$NH_4^+ + NO_2^- \rightarrow N_2 + 2\,H_2O, \qquad [15]$$

which has been proven to be valid for zeolite structures in their ammonium form (17), proceeds even on the alkali form of the zeolites. It could be shown by *in situ* FTIR experiments (41) that during interaction of NO_x with the surface of the composite catalyst 15 $MnNaY_{775}$, the characteristic vibration bands of zeolitic Brønsted acid sites emerge. These Brønsted acid sites are formed during the interaction of zeolite NaY with NO_x in the presence of water, indicating an *in situ* exchange of Na^+ ions by H^+ at Al-O^--Si units of the zeolite framework. Thus, formation of NH_4^+ ions from NH_3 can take place during reaction. DRIFT spectroscopic measurements revealed the *in situ* formation of hydroxyls located at manganese ions. The role of these hydroxyl

groups and how far they interact with ammonia cannot be stated at present. It is unlikely that the concentration and acid strength of detected Mn–OH groups are sufficiently high to ensure NH_3 activation as NH_4^+ ions, as is reported for V–OH groups of the V/TiO_2 SCR catalyst (45). The predominance of Lewis acid sites on the MnO_x/NaY composite implies an activation of ammonia by dissociation, forming amide species with concomitant hydrogen transfer to adjacent oxygen atoms, as reported for other oxides (45). This is denoted the "amide/nitrosamide" SCR reaction route, proposed for NO_x conversion by NH_3 over 2 wt% Mn/Al_2O_3 catalysts (35). But as follows from data given in Table 4, these and other Mn-based catalyst formulations do not achieve comparable activities to the 15 MnNaY catalyst with wet feed. Impregnation of nonzeolitic supports with Mn salt solutions and calcination of the catalyst lead to the emergence of crystalline Mn oxides which are not as active and selective as the amorphous MnO_x bulk phase on the microporous zeolite. Whereas the MnO_x phase precipitated on zeolite NaY retains its amorphous state with mainly tetravalent manganese after catalyst calcination at 775 K, MnO_x precipitated in the absence of the zeolite is mostly converted to crystalline α-MnO_2 and γ-Mn_2O_3 after calcination at 775 K. Correspondingly, the catalytic behavior of sample Mn_{775} is characterized by moderate NO_x conversion activity and a high N_2O by-product formation (cf. Fig. 11A), as is characteristic for crystalline manganese oxides (25) and also for manganese oxides supported on Al_2O_3 at higher loading (36).

Due to its favorable pore structure, zeolite NaY is able to stabilize and to store NO_x in the form of nitrate, nitrite, and N_2O_3-like intermediates. The performance of the composite catalyst 15 $MnNaY_{775}$ is related to the close neighborhood of the catalyst components coupling nitrite formation and its drain off from equilibria with NO/NO_2 and nitrate by activated ammonia. Redox properties of MnO_x promote oxidation of NO to NO_2, and the ion exchange properties of the zeolite, besides its Lewis acidity, allows reaction pathways of NO_x reduction by both the diazotation and the amide/nitrosamide mechanism.

CONCLUSIONS

The applied precipitation technique for preparation of a composite material with intended egg-shell arrangement of amorphous MnO_x around zeolite NaY microcrystals leads to catalysts with high performance in the SCR of NO_x by NH_3. The catalyst tolerates water contents of up to 30 vol% in the feed. Full conversion of NO_x is achievable at 325–450 K up to GHSV values of ca. 50,000 $cm^3\,g_{cat}^{-1}\,h^{-1}$ in the presence of 5–10 vol% water.

The most relevant feature of the composite MnO_x/NaY catalyst is its high activity at temperatures where commercial $V_2O_5/WO_3/TiO_2$ catalysts are only marginally active (46).

These properties would fulfill the requirements of a low-temperature NO_x reduction catalyst for mobile diesel engines if an ammonia supply is implemented "on board," e.g., by urea decomposition.

ACKNOWLEDGMENTS

The authors are indebted to U. Wolf and R. Eckelt for technical assistance. The work was supported by the Federal Ministry for Education and Research of the FRG and the Senate of Berlin (project 03C3005). M.R. and R.F. wish to thank the Verband der Chemischen Industrie (VCI) for financial support.

REFERENCES

1. Janssen, F. J., *in* "Handbook of Heterogeneous Catalysis" (G. Ertl, H. Knözinger, and J. Weitkamp, Eds.), Vol. 4, p. 1633. VCH, Weinheim, 1997.
2. Parvulescu, V. I., Grange, P., and Delmon, B., *Catal. Today* **46**, 233 (1998).
3. Forzatti, P., *Catal. Today* **62**, 51 (2000).
4. Held, W., König, A., Richter, T., and Puppe, L., *Technical Paper Series 900496*. Society of Automotive Engineers, Warrendale, 1990.
5. Amon, B., Fischer, S., Hofman, L., and Zürbig, J., *in* "Preprints of the Fifth International Congress on Catalysis and Automotive Pollution Control," Brussels, April 12–14, 2000, Vol. 1, 215. Universite Libre de Bruxelles, Brussels, 2000.
6. Koebel, M., Elesener, M., and Kleemann, M., *Catal. Today* **59**, 335 (2000).
7. Jacob, E., EP 0487886 B1, MAN Technologie AG, Munich (1994).
8. Stevenson, S. A., Vartuli, J. C., and Brooks, C. F., *J. Catal.* **190**, 228 (2000).
9. Eng, J., and Bartholomew, C. H., *J. Catal.* **171**, 14 (1997).
10. Roberge, D., Raj, A., Kaliaguine, S., On, D. T., Iwamoto, S., and Inui, T., *Appl. Catal. B* **10**, L237 (1996).
11. Andersson, L. A. H., Brandin, J. G. M., and Odenbrand, C. U. I., *Catal. Today* **4**, 173 (1989).
12. Odenbrand, C. U. I., Andersson, L. A. H., Brandin, J. G. M., and Järas, S., *Catal. Today* **4**, 155 (1989).
13. Brandin, J. G. M., Andersson, L. A. H., and Odenbrand, C. U. I., *Catal. Today* **4**, 187 (1989).
14. Choi, E.-Y., Nam, I.-S., and Kim, Y. G., *J. Catal.* **161**, 597 (1966).
15. Medros, F. G., Eldridge, J. W., and Kittrell, J. R., *Ind. Eng. Chem. Res.* **28**, 1171 (1989).
16. Kieger, S., Delahay, G., Coq, B., and Neveu, B., *J. Catal.* **183**, 267 (1999).
17. Richter, M., Eckelt, R., Parlitz, B., and Fricke, R., *Appl. Catal. B* **15**, 129 (1998).
18. Richter, M., Berndt, H., Eckelt, R., Schneider, M., and Fricke, R., *Catal. Today* **54**, 531 (1999).
19. Richter, M., Kosslick, H., and Fricke, R., *Stud. Surf. Sci. Catal.* **130**, 1517 (2000).
20. Barrett, E. P., Joyner, L. S., and Halenda, P. P., *J. Am. Chem. Soc.* **73**, 373 (1951).
21. Veprek, S., Sarott, F.-A., and Iqbal, Z., *Phys. Rev. B* **36**, 3344 (1987).
22. R. J. Meyer, Ed. "Gmelins Handbuch der Anorganischen Chemie," Vol. 56, Part C1, p. 126, Verlag Chemie, Weinheim 1973.
23. Buciuman, F., Patcas, F., Cracium, R., and Zahn, D. R. T., *Phys. Chem. Chem. Phys.* **1**, 185 (1999).
24. Bernard, M.-C., Hugot-Le Goff, A., Thi, B. V., and Cordoba de Terresi, S., *J. Electrochem. Soc.* **140**, 3065 (1993).

25. Kapteijn, F., Singoredjo, L., and Andreini, A., *Appl. Catal. B* **3**, 173 (1994).
26. Hadjiivanov, K., *Catal. Rev.–Sci. Eng.* **42**, 71 (2000).
27. Nakamoto, K., "IR and Raman Spectra of Inorganic and Organic Compounds," 3rd ed. Wiley, New York, 1978.
28. Kapteijn, F., Singoredjo, L., Dekker, N. J. J., and Moulijn, J. A., *Ind. Eng. Chem. Res.* **32**, 445 (1993).
29. Hadjiivanov, K., Saussey, J., Freysz, J.-L., and Lavalley, J.-C., *Catal. Lett.* **52**, 103 (1998).
30. Varetti, W. L., and Pimentel, G. C., *J. Phys. Chem.* **55**, 3813 (1971).
31. Aylor, A. W., Lobree, L. J., Reimer, J. A., and Bell, A. T., *J. Catal.* **170**, 390 (1997).
32. Kijlstra, W. S., Daamen, J. C. M. L., van de Graaf, J. M., van der Linden, B., Poels, E. K., and Bliek, A., *Appl. Catal. B* **7**, 337 (1996).
33. Kijlstra, W. S., Brands, D. S., Poels, E. K., and Bliek, A., *J. Catal.* **171**, 208 (1997).
34. Kijlstra, W. S., Brands, D. S., Smit, H. I., Poels, E. K., and Bliek, A., *J. Catal.* **171**, 219 (1997).
35. Kijlstra, W. S., Brands, D. S., Poels, E. K., and Bliek, A., *Catal. Today* **50**, 133 (1999).
36. Kapteijn, F., Singoredjo, L., van Driel, M., Andreini, A., Moulijn, J. A., Ramis, G., and Busca, G., *J. Catal.* **150**, 105 (1994).
37. Kijlstra, W. S., Poels, E. K., Bliek, A., Weckhuysen, B. M., and Schoonheydt, R. A., *J. Phys. Chem. B* **101**, 309 (1997).
38. Grzybek, T., Klinik, J., Krzyzanowski, A., Papp, H., and Zyla, M., *Catal. Lett.* **63**, 107 (1999).
39. Halasz, I., Brenner, A., and Ng, K. Y. S., *Catal. Lett.* **34**, 151 (1995).
40. Amblard, M., Burch, R., and Southward, B. W. L., *Catal. Lett.* **68**, 105 (2000).
41. Bentrup, U., Brückner, A., Richter, M., and Fricke, R., *Appl. Catal. B* **32**, 229 (2001).
42. Sultana, A., Loenders, R., Monticelli, O., Kirschhock, C., Jacobs, P. A., and Martens, J. A., *Angew. Chem.* **112**, 112 (2000).
43. Szanyi, J., and Paffett, M. T., *J. Catal.* **164**, 232 (1996).
44. Raj, A., Le, T. H. N., Kaliaguine, S., and Auroux, A., *Appl. Catal. B* **15**, 259 (1998).
45. Busca, G., Lietti, L., Ramis, G., and Berti, F., *Appl. Catal. B* **18**, 1 (1998).
46. Richter, M., *et al.*, unpublished results.